

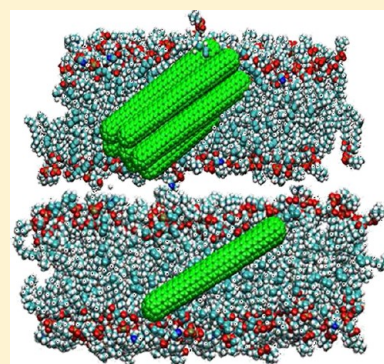
# Embedded Single-Walled Carbon Nanotubes Locally Perturb DOPC Phospholipid Bilayers

R. Parthasarathi,<sup>†</sup> N. R. Tummala,<sup>‡</sup> and A. Striolo<sup>\*,†</sup>

<sup>†</sup>The School of Chemical, Biological and Materials Engineering, The University of Oklahoma, Norman, Oklahoma 73019, United States

<sup>‡</sup>School of Chemistry and Biochemistry, Georgia Institute of Technology, Atlanta, Georgia 30332, United States

**ABSTRACT:** Understanding and controlling how carbon nanotubes interact with phospholipid membranes is necessary for preventing adverse effects of these relatively new, but still exciting, materials. Futuristic applications envision incorporating carbon nanotubes in liposomes for personalized medicine, controlled delivery, and imaging. Because of their ability to penetrate phospholipid bilayers, nanotubes could serve as nanoscale syringes to deliver molecular cargo and develop gene therapy. Several experimental reports available on the subject demonstrate the need for a better understanding, at the molecular level, of whether carbon nanotubes penetrate, reside, and perturb phospholipid bilayers. Using all-atom molecular dynamics simulations, we quantify how short carbon nanotubes (~6 nm in length) embedded within a DOPC phospholipid membrane perturb the structure, organization, and dynamics of the lipid molecules within the membrane. It is found that the structural perturbation is very short-ranged, although it becomes pronounced when bundles of carbon nanotubes are formed within the membrane. The presence of the nanotubes is found to reduce the mobility of lipid molecules within the membrane and to perturb the structure of interfacial water. Our observations suggest that the local perturbations in the lipid structure caused by the nanotubes could lead to enhanced penetration of molecular compounds across the membrane.



## 1. INTRODUCTION

Carbon nanotubes (CNTs) not only show impressive intrinsic properties for a number of technological applications but also attract interest for the delivery of diagnostics and therapeutic material at the cellular level.<sup>1,2</sup> As a futuristic example, Chen et al.<sup>3</sup> used one CNT, immobilized on an AFM tip, to insert “molecular cargo” through phospholipid membranes. Other possible biological/biomedical applications of CNTs include ultrasensitive sensors, nanocomposites for neural and orthopedic devices, and delivery systems.<sup>4</sup> Because these applications take advantage of the CNTs’ size, it is important to remember that single-walled carbon nanotubes (SWNTs) have diameters in the range of 0.4–2.0 nm and lengths up to a few micrometers, whereas multiwalled carbon nanotubes (MWNTs) have diameters and lengths up to 100 nm and several micrometers, respectively.<sup>5</sup> Experimental data suggest that CNTs can deliver drugs, antigens, and genes into both prokaryotic and mammalian cells<sup>6–11</sup> because CNTs readily traverse the plasma membrane and enter the cell cytoplasm. CNTs translocate the plasma membrane of human cell lines, including HeLa and epithelial carcinoma cells.<sup>12,13</sup> Non-functionalized MWNTs have been found to cross the lysosomal membrane of mature human monocyte-derived macrophages.<sup>14,15</sup>

The initial enthusiasm in employing CNTs for medical applications was, however, mitigated by reports on their toxicity, as well as on concerns regarding the expected extended lifetime of such compounds. Regarding biodegradability, Star

and co-workers recently reported the catalytic biodegradation of carboxylated SWNTs via horseradish peroxidase in the presence of H<sub>2</sub>O<sub>2</sub>.<sup>16,17</sup> SWNTs have also been degraded in fluids that mimic the phagolysosome milieu.<sup>18</sup> Defects present on the CNTs and their degree of carboxylation affect the kinetic of decomposition.<sup>19,20</sup> Functionalized SWNTs can also be degraded inside neutrophils and macrophages.<sup>21</sup> Bianco et al.<sup>22</sup> provided an interesting and rather complete review on the subject.

Even more extensive is the literature on possible CNT cytotoxicity. Initial literature reports suggested that SWNTs exhibit cytotoxicity to human<sup>23,24</sup> and animal cells,<sup>25,26</sup> whereas MWNTs, with a lower surface-to-volume ratio, have been shown to yield much milder, when detected, toxicological effects.<sup>27</sup> Careful analysis has, however, indicated the use of CNT samples of different purities, aggregation states, and functionalizations,<sup>26–29</sup> and also differences in the choice of cell-culture media and cell type.<sup>12,30</sup> For example, Crouzier et al.<sup>31</sup> reported that SWNT purification significantly reduces the lytic effect on red blood cells. Recent investigations tend to be very rigorous in the characterization of the CNTs employed. Wick et al.<sup>29</sup> reported in vitro cytotoxicity results conducted with the mesothelioma cell line MSTO-211H. They considered CNTs dispersed using the noncytotoxic polyoxyethylene

**Received:** June 26, 2012

**Revised:** September 27, 2012

**Published:** October 1, 2012



sorbitan monooleate, and they found that small, suspended CNT bundles had less cytotoxicity than asbestos, but that micrometer-sized ropelike CNT agglomerates had more cytotoxicity than asbestos at similar concentrations. Mutlu et al.<sup>32</sup> exposed human alveolar cells from line A549, and intracheally administered SWNTs, either well-dispersed or agglomerated, to mice. To disperse the SWNTs, they used the biocompatible block copolymer Pluronic F 108NF. Regarding the A549 cells, the authors found minimal effects when compared to the effects of particles associated with known adverse health effects (asbestos); regarding mice, 30 days after administration, evidence of granuloma-like structures with mild fibrosis was found in the large airways, but only when the SWNTs were agglomerated. The results suggested that nanoscale-dispersed SWNTs were taken up by alveolar macrophages and cleared from the lung over time.

Elimelech and co-workers<sup>33</sup> conducted a comparative study regarding the microbial cytotoxicity of various carbon-based nanoparticles, finding enhanced SWNT antimicrobial activity. They also assessed the antibacterial effects of well-purified and characterized CNTs toward *Escherichia coli*.<sup>34</sup> The results suggested that SWNTs are much more toxic than MWNTs. An interesting follow-up study by Vecitis et al.<sup>35</sup> took advantage of recent developments in density gradient ultracentrifugation techniques for the separation of metallic and semiconductive SWNTs of similar length and diameter. When samples containing <5%, ~30%, or >95% metallic SWNTs were placed at contact with *E. coli*, the cytotoxicity was found to increase with the fraction of metallic SWNTs. Further analysis showed that increasing the fraction of metallic SWNTs in the sample increases the extent of glutathione oxidation. Glutathione is an intracellular antioxidant and redox mediator. These results suggest that SWNTs' antimicrobial mechanism follows three steps: SWNT–bacteria contact, perturbation of the cell membrane, and oxidation of cellular compounds.

Although chemical functionalization appears to alleviate the cytotoxicity of CNTs, surfactants may not provide such a relief. Liu et al.<sup>36</sup> compared the CNTs' effects on the gram-negative bacteria *E. coli* and *Pseudomonas aeruginosa*, and on the gram-positive *Staphylococcus aureus* and *Bacillus subtilis*. They used SWNTs carefully characterized and dispersed in saline solutions, as well as in solutions containing Tween 20 or sodium cholate surfactants. The SWNTs in saline solutions without surfactants were found to aggregate in bundles. The Tween 20 surfactant was found not to be cytotoxic, whereas sodium cholate was found to decrease the bacteria survival rate. Exposition to the SWNTs was found to increase the death rate for all bacteria, although the gram-positive bacteria were more affected than the gram-negative ones. The results also showed that individually dispersed SWNTs are more efficient antimicrobial agents than bundles. The mode of action was found to be primarily cell membrane piercing. The authors argued that, because individually dispersed SWNTs can travel faster than the bundles, they affect more bacteria. It remains to be understood why chemical functionalization of the CNTs reduces their cytotoxicological properties, whereas physical functionalization using surfactants does not yield similar effects.

Regarding CNTs as drug-delivery agents, experiments suggest, maybe not surprisingly, that the type of CNT functionalization affects cellular uptake, possibly changing the uptake mechanism.<sup>9,37</sup> Singh et al.<sup>38</sup> synthesized 12 polyamine-modified SWNTs and MWNTs, most of which showed reduced cytotoxicity for human lung epithelial A549 cells

exposed to the CNTs for 24 and 72 h. Some of these CNTs managed to efficiently complex siRNA, as assessed by gel electrophoresis, and were internalized by A549 cells, suggesting the possibility of using these materials for gene delivery and silencing. In an attempt to discriminate between different uptake mechanisms, Al-Jamal et al.<sup>13</sup> employed functionalized MWCNTs (MWNT-NH<sub>3</sub><sup>+</sup>) with diameters of ~20–30 nm and lengths of 50–500 nm and placed them in contact with either A549 cells or primary macrophages at 4 and 37 °C. The A549 cells were chosen because they are almost incapable of phagocytosis, while macrophages are capable of efficient phagocytosis. The experiments at 4 °C were performed to decrease the likelihood of phagocytosis. Three-dimensional electron tomography imaging showed CNT internalization in both cell lines according to three mechanisms: (a) individual CNT uptake via membrane wrapping, (b) direct membrane translocation of individual CNTs, and (c) internalization of CNT clusters with the formation of vesicular compartments. Data analysis after 14 days confirmed that the functionalized CNTs were able to escape vesicular entrapment, presumably by translocation of individual CNTs into the cytoplasm.

The results summarized above suggest that significant progress is being made in understanding how CNTs interact with living cells, and how such interactions could be deployed for advanced applications, such as antimicrobial processes and personal medicine. In all of these applications, CNTs come in contact with phospholipid bilayers, which have been designed by nature to separate interior and exterior environments for cells.<sup>39</sup> Designing delivery methods to penetrate this protective barrier without altering the chemical–physical properties of drugs or other molecular cargo (e.g., genes) could lead to tools for the transmembrane delivery of selective compounds.<sup>40</sup> The main obstacle for achieving such a goal is a detailed understanding of how nanoscale objects interact with the phospholipid bilayers.<sup>41–43</sup>

Phospholipid bilayers, in the form of liposomes, are among the systems most often used clinically to control the delivery of cytotoxic and antifungal drugs, genes, vaccines, and imaging agents.<sup>44</sup> Other models of biological membranes include supported phospholipid bilayers.<sup>45</sup> Al-Jamal and Kostarelos<sup>46</sup> reviewed recent progress in “theranostic nanomedicine”. Rash et al.<sup>47</sup> produced and characterized phosphatidylcholine lipid vesicles embedded with sub-2-nm diameter dodecanethiol-coated gold nanoparticles. Should CNTs be used in theranostic medicine, a detailed understanding of the structure of the phospholipid membrane with embedded CNTs is required. Simulation studies at various length scales are likely to aid such characterization.

For example, a number of detailed theoretical studies have been conducted to investigate the interaction between carbon-based nanoparticles and phospholipid bilayers, and the uptake of different nanomaterials by a phospholipid membrane. Lopez et al.<sup>48</sup> considered a short generic nanotube characterized by hydrophilic groups at the pore openings and used molecular simulations to observe the spontaneous adsorption of this tube within a phospholipid bilayer. The resultant complex provided a phospholipid membrane with embedded transmembrane nanopores. Yang and Ma<sup>49</sup> employed dissipative particle dynamics to study how nanoparticles of different shapes (spheres, ellipsoids, rods, discs, and pushpin-like) penetrate a phospholipid bilayer. The results suggest that the shape anisotropy and the orientation of the particle when it comes in contact with the membrane are crucial for determining the

nature of the particle–membrane interactions. Other important parameters include the initial contact area, the particle curvature at the membrane–particle contact region, and particle rotation. Frenkel and co-workers<sup>50</sup> simulated the process of passive endocytosis using coarse-grained molecular dynamics. The results showed that passive endocytosis becomes possible as the nanoparticles are coated by a sufficiently large concentration of ligands and that it is more efficient for spherocylindrical particles than for spherical ones; endocytosis is suppressed for particles with sharp edges. Redmill and McCabe<sup>51</sup> compared the free energy profile experienced by  $C_{60}$  as it penetrates a phospholipid bilayer to that experienced by one polyhedral oligomeric silsesquioxane, another emerging nanomaterial.<sup>52</sup> Song et al.<sup>53</sup> employed coarse-grained simulations to investigate the penetration of nanocrystals with a size in the 1.0–2.0 nm range through DPPC bilayers. They monitored the minimal force necessary for the nanocrystal to penetrate the bilayer, as well as changes in membrane structure (e.g., thickness and lipid order parameter) and mechanical properties during the process. Wallace and Sansom<sup>54</sup> simulated one CNT moving across a dipalmitol-phosphatidylcholine (DPPC) bilayer and found that the CNT extracts lipid molecules as it pierces the membrane.

Several investigations addressed the adsorption of fullerenes in phospholipid bilayers. D’Rozario et al.<sup>55</sup> calculated free energy profiles for  $C_{60}$  molecules characterized by different surface functionalizations. When the surface is predominantly hydrophobic, the fullerenes are found to spontaneously embed within the phospholipid bilayer, whereas, when the surface is largely functionalized with –OH groups, the fullerenes preferentially reside in contact with, but outside of, the phospholipid bilayer. Jusufi et al.<sup>56</sup> employed all-atom and coarse-grained simulations to investigate the adsorption of  $C_{60}$ – $C_{540}$  molecules in phospholipid bilayers and the perturbation of the membrane structure as a function of the fullerene concentration. They found that the adsorption process is thermodynamically favored, and limited only by diffusion. The penetration mechanism changes depending on the carbon particle size, with larger particles yielding a distortion of the lipid molecules as they enter the bilayer. The authors also quantified the mobility of the embedded fullerenes in terms of diffusion coefficients and used coarse-grained simulations to study the fullerene self-assembly within the membrane. Significant perturbation of the membrane structure was reported. Bedrov et al.<sup>57</sup> employed atomistic simulations to detail the penetration of one  $C_{60}$  in a fully hydrated dimyristoyl-phosphatidylcholine (DMPC) bilayer. It was found that  $C_{60}$  easily penetrates the lipid bilayer (no free energy barriers were observed) because of stronger dispersive interactions between  $C_{60}$  and lipid molecules in the membrane than between  $C_{60}$  and water. Because of excluded-volume effects, the membrane was found to be slightly distorted in its thickness when the  $C_{60}$  was embedded. Qiao et al.<sup>58</sup> investigated the penetration of one  $C_{60}$  and that of one  $C_{60}(\text{OH})_{20}$  in DPPC bilayers. They found that  $C_{60}$  is readily embedded within the membrane, whereas  $C_{60}(\text{OH})_{20}$  remains in contact with the membrane but does not spontaneously penetrate it. As either of the two fullerenes approaches the membrane, the structure of the lipid molecules changes. In the case of  $C_{60}$ , the lipids get further from each other, almost yielding a small pore, whereas in the case of  $C_{60}(\text{OH})_{20}$ , the lipids pack closer to each other, providing steric hindrance to fullerene penetration. Monticelli and co-workers<sup>59</sup> investigated

how several  $C_{60}$  fullerenes penetrate a phospholipid bilayer. The results showed that the fullerenes aggregate in the bulk aqueous solution, but they disaggregate and disperse as they penetrate the phospholipid bilayer (note that experiments suggest that fullerenes aggregate when embedded in a membrane<sup>60</sup>). Changes in membrane structure and elastic properties were detected in the presence of  $C_{60}$ , but they were not sufficient to suggest that the membrane would fail because of the fullerenes.

Fewer studies, although this literature is growing quickly, describe the interaction between CNTs and phospholipid bilayers. Pogodin and Baulin<sup>60</sup> employed the single-chain mean field theory<sup>61</sup> to investigate the free energy profile experienced by a CNT, envisioned as a rigid cylinder, as it pierces a bilayer. The results showed that some CNTs could create a pore as they penetrate the bilayer (hydrophilic CNTs) and others could penetrate without significantly perturbing the membrane structure (hydrophobic CNTs). Because CNTs can be “decorated” via the adsorption of several compounds (surfactants, proteins, DNA, polymers, maybe even lipids, etc.), Pogodin et al.<sup>62</sup> considered CNTs whose surface was patterned by hydrophobic and hydrophilic stripes. For some of the patterns considered, the free energy profile remained approximately constant as the CNTs penetrated a phospholipid membrane, suggesting that piercing can be facilitated by appropriate functionalization of the CNTs. Hofinger et al.<sup>63</sup> recently combined the membrane mimicry approach<sup>64</sup> and dissipative particle dynamics<sup>65</sup> simulations to study CNT adsorption into phospholipid bilayers. The CNTs considered were of different lengths, individually dispersed, as well as assembled in bundles. In all cases, the nanotubes were not functionalized. The nanotubes were found to preferentially reside within the membrane, in agreement with the simulations discussed above. When the CNTs are short, they were found to align parallel to the lipid molecules (perpendicular to the membrane), but as their length increases, the CNTs preferentially assembled parallel to the membrane. The results also suggested that the membrane promotes the formation of CNT bundles with structures somewhat different than those observed in vacuum.

As a complement to the investigations summarized above, the structure of lipid molecules, as well as that of common surfactants, self-assembled onto SWNTs of various diameters has also been investigated via molecular simulations,<sup>66–70</sup> yielding results that are in good agreement with experimental observations.<sup>71</sup>

As this review shows, a number of literature simulation studies describe interactions between CNTs and phospholipid membranes. What is still missing, which will be important for the development of theranostic nanomedicine, is a molecular-level understanding of how a phospholipid membrane changes upon the adsorption of CNTs. Improving this understanding is the scope of the present paper.

This work builds on the significant literature available for phospholipid bilayers. Among experimental data, the NMR results reported by Warschawski and Devaux<sup>72</sup> for the structure of phospholipid bilayers and the diffuse X-ray scattering results reported by Liu and Nagle<sup>73</sup> for structural quantities, such as the area per lipid at the interface, will be used to validate our simulation protocol. Our study also builds on results reported in the literature for lipid<sup>74,75</sup> and phospholipid bilayers.<sup>76–78</sup> As the models implemented improve and the computational power available to researchers continues to expand, the



simulation results yield more and more interesting insights. For example, Lim and Klaudas<sup>79</sup> simulated membranes composed of lipid molecules found in the intracellular eubacterial parasite *Chlamidia trachomatis* and found that branching in the lipid molecule increases the average lipid surface area, membrane elastic moduli, and lipid axial relaxation times, while decreasing the lipid chain order. Vanegas et al.<sup>80</sup> quantified the modulation of lateral and normal pressure profiles due to the addition of ergosterol to a DPPC bilayer, and Skaug et al.<sup>81</sup> showed that even small concentrations of fluorescent probes can have a significant impact on the properties of a lipid bilayer.

This paper is organized as follows. In section 2, we briefly summarize the simulation methods employed. In section 3, we analyze the results, and in section 4, we briefly summarize the main results.

## 2. SIMULATION METHODS AND ALGORITHMS

All-atom molecular dynamics simulations were employed to detail the structure of a phospholipid bilayer and how such a structure changes upon CNT adsorption. The simulation protocol adopted follows procedures established in the literature.<sup>82</sup> The lipid molecule chosen for our studies is dioleoylphosphatidylcholine (DOPC). One DOPC lipid molecule is composed of one hydrophilic head and two hydrophobic tails. The hydrophilic head is composed of choline ( $-\text{NC}_5\text{H}_{13}$ ), phosphate ( $-\text{PO}_4$ ), and glycerol groups ( $-\text{C}_5\text{H}_5\text{O}_5$ ). Each of the two hydrophobic tails (indicated as  $\text{sn}_1$  and  $\text{sn}_2$ ) is composed of 18 carbon atoms. A representative snapshot of one DOPC molecule is shown in Figure 1.

The lipid bilayer considered consists of 288 DOPC molecules, distributed among two leaflets, each containing 144 lipid molecules. The simulation box contained 10 908 water molecules. The lipid bilayer–water system was equilibrated for 100 ns in the NP $\gamma$ T ensemble. The surface

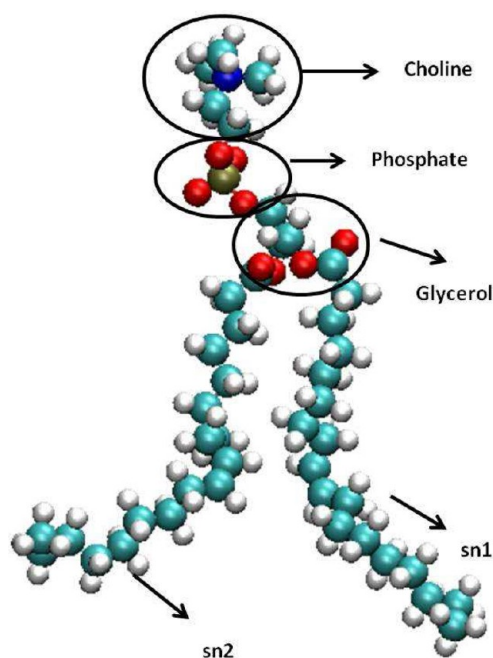


**Figure 1.** Schematic representation of one DOPC lipid molecule. Highlighted are the choline, phosphate, and glycerol groups that compose the lipid hydrophilic head, as well as the two hydrophobic tails ( $\text{sn}_1$  and  $\text{sn}_2$ ), each composed of 18 carbon atoms.

tension was maintained at 22 dyn/cm to reproduce the experimental surface area per headgroup,<sup>81</sup> at a temperature and pressure of 310 K and 1 bar. The bilayer–water system was considered to reach equilibrium when the surface tension fluctuates around the desired constant value. The equilibrated simulation box size is  $\sim 10.0 \times 10.0 \times 8.2 \text{ nm}^3$ . These values change when CNTs are inserted. The NP $\gamma$ T ensemble with a surface tension of 22 dyn/cm was used for all equilibration and production runs even after carbon nanotubes were inserted into the bilayer. Following prior simulations<sup>82</sup> and experimental suggestions,<sup>83</sup> the water-to-lipid ratio used in our simulations is 37.9. A representative snapshot of the simulated water–bilayer system is shown in Figure 2a (system A).

From the equilibrated system just described, initial configurations were created to study phospholipid bilayers with embedded CNTs. Three configurations were created. In all cases, 6 nm long capped (5,5) CNTs were used. In the first configuration, one CNT was placed parallel to the bilayer (Figure 2b, system B); in the second one, one CNT was placed perpendicular to the bilayer (Figure 2c, system C); and in the third, one bundle of seven CNTs was placed perpendicular to the bilayer (Figure 2d, system D). In Table 1, we report the composition and other details for each of the systems considered in this work. All of these systems were first equilibrated for 100 ns. The total simulation run was as long as 300 ns for each system considered.

DOPC molecules were modeled with the general all-atom AMBER force field (GAFF),<sup>82</sup> which explicitly considers hydrogen atoms. Water molecules were modeled by the simple point charge-extended (SPC/E) model.<sup>84</sup> The carbon atoms in the CNTs were simulated using the universal force field (UFF).<sup>85</sup> Interactions among carbon atoms of different CNTs were described using Lennard-Jones potentials of Cheng and Steele.<sup>86</sup>

Following literature,<sup>82</sup> all interactions were cut off at the distance of 1 nm. Long-range electrostatic interactions were treated using the particle mesh Ewald summation method.<sup>87</sup>

## 3. RESULTS AND DISCUSSION

**DOPC Bilayer.** To ensure that the implemented model satisfactorily yields the structural properties for the DOPC bilayer, we compute important quantities, such as membrane thickness, surface area per lipid molecule, and deuterium order parameter. After equilibration, the area per lipid is found to be  $70.0 \pm 0.2 \text{ \AA}^2$ , in good agreement with other simulations ( $72 \text{ \AA}^2$ , ref 82) and with experimental data ( $72.1 \text{ \AA}^2$ , ref 83). The bilayer thickness of the DOPC lipid membrane for our system is  $36.4 \pm 0.2 \text{ \AA}$ , also in good agreement with prior simulation and experimental data ( $36.1$  and  $37.1 \text{ \AA}$ , respectively).<sup>82,83</sup> The deuterium order parameter is used to determine the average structure of the lipid molecules within the bilayer.<sup>88</sup> The results for the DOPC bilayer as a function of carbon atoms in the tail of the lipid are presented in Figure 3. Blue and red lines are for  $\text{sn}_1$  and  $\text{sn}_2$  chains of the lipid molecule, respectively. For both the chains ( $\text{sn}_1$  and  $\text{sn}_2$ ), the order parameter is higher for the carbon atoms near the glycerol group (carbon atoms C1–C5), and it gradually decreases when the carbon atoms are farther from glycerol (C6–C9). A minimum in the order parameter, indicative of a more disordered structure, is found between carbon atoms C9 and C10, corresponding to the double bond. Before the minimum, the data suggest that the  $\text{sn}_1$  chain is more ordered than the  $\text{sn}_2$  chain. After the minimum, the order parameter increases slightly for carbon atoms C10–C12,

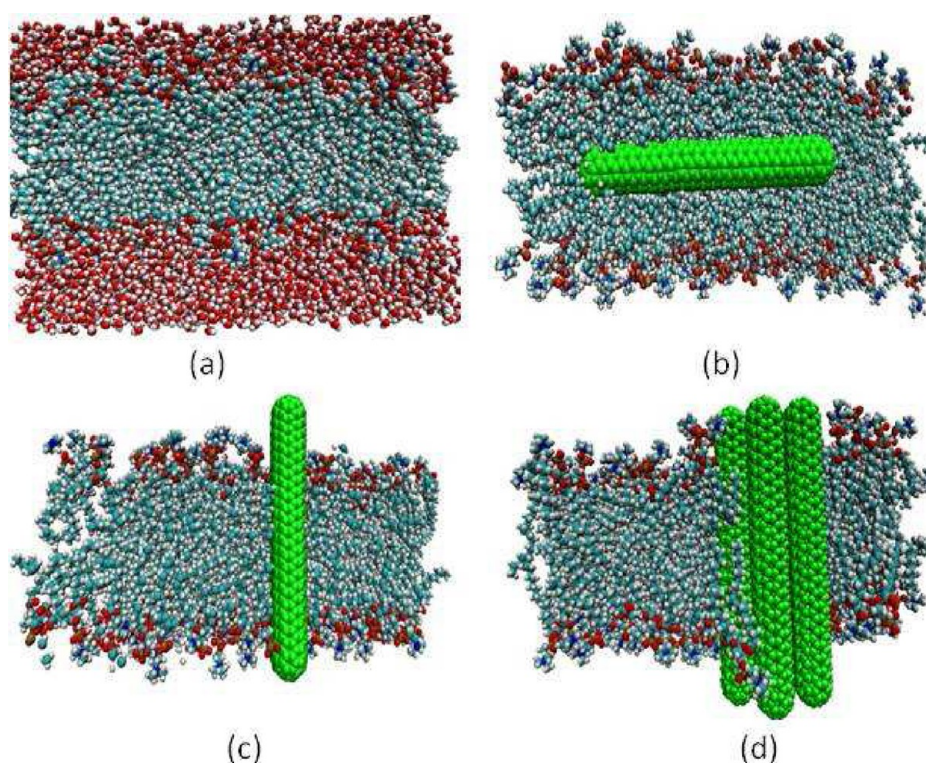


**Figure 2.** Representative simulation snapshots of the four systems considered in this work. (a) Equilibrated DOPC bilayer in water without CNTs (system A). (b) Lipid bilayer with one CNT parallel to the bilayer (system B). (c) Lipid bilayer with one CNT perpendicular to the bilayer (system C). (d) Lipid bilayer with one bundle of seven CNTs perpendicular to the bilayer (system D). Panel (a) is for an equilibrated system, whereas the other panels are initial configurations. Water molecules are not shown in panels (b)–(d) for clarity. Green spheres represent carbon atoms in CNTs, blue spheres represent carbon atoms in the lipid bilayer, red spheres represent oxygen in water and in the DOPC headgroup, and white spheres represent hydrogen atoms in water and DOPC.

**Table 1. Composition and Simulation Box Size at Equilibrium of the Simulated Systems**

	number of water molecules	number of DOPC molecules	simulation box size (nm <sup>3</sup> )
system A: no CNT	10 908	288	10.0 × 10.0 × 8.2
system B: one CNT parallel to the lipid bilayer	10 908	288	10.0 × 10.0 × 8.2
system C: one CNT perpendicular to the lipid bilayer	16 905	266	9.74 × 9.42 × 9.42
system D: bundle of 7 CNTs perpendicular to the lipid bilayer	16 905	266	9.70 × 10.13 × 9.20

because of gauche effects, after which it remains approximately constant until the C16 carbon atom. Differences between results for the  $sn_1$  and  $sn_2$  chains are due to the fact that  $sn_1$  is oriented more perpendicular to the membrane, and  $sn_2$  parallel to it, as expected, given the structure of one DOPC molecule (see Figure 1). The results obtained are in good agreement with both simulation<sup>82</sup> and experimental data.<sup>83</sup> Vermeer et al.,<sup>89</sup> in an interesting review, provided additional elements to interpret deuterium order parameter results.

**Orientation of the Embedded CNTs.** The simulation results by Höfinger et al.<sup>63</sup> suggest that short CNTs ( $\sim 2$  nm in length) embedded within a phospholipid bilayer orient preferentially parallel to the lipid molecules and that, as the CNTs' length increases ( $\sim 7$  nm), the CNTs lie in the middle of the bilayer, parallel to the bilayer itself (perpendicular to the

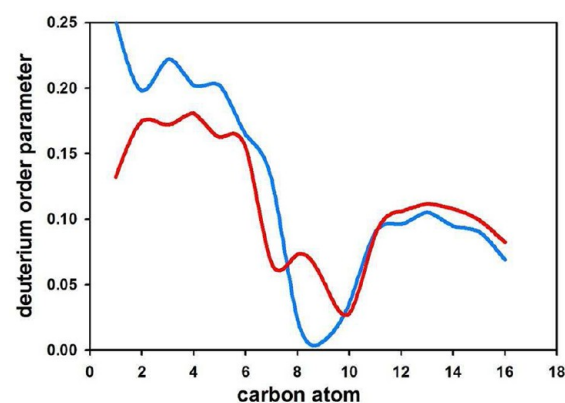


**Figure 3.** Averaged deuterium order parameter obtained for the DOPC bilayer in water. Blue and red lines are for  $sn_1$  and  $sn_2$  tails, respectively (see Figure 1 for a schematic).

lipid molecules). In our simulations, the CNTs are free to move, within the limits accessible via atomistic molecular dynamics. From the initial configurations shown in Figure 2, panels (b)–(d) (systems B–D, respectively), we conducted simulations for up to 300 ns to monitor changes in the CNTs' orientation. It is expected that the single CNT parallel to the bilayer, system B, remains in that orientation as the simulation progresses. In systems C and D, the single CNT and the CNT bundle are both expected to tilt so that the hydrophobic carbon nanotube surfaces are completely buried within the hydrophobic part of the bilayer. In Figure 4, we report results, as a function of time, for the tilt angle formed by the CNT axis and



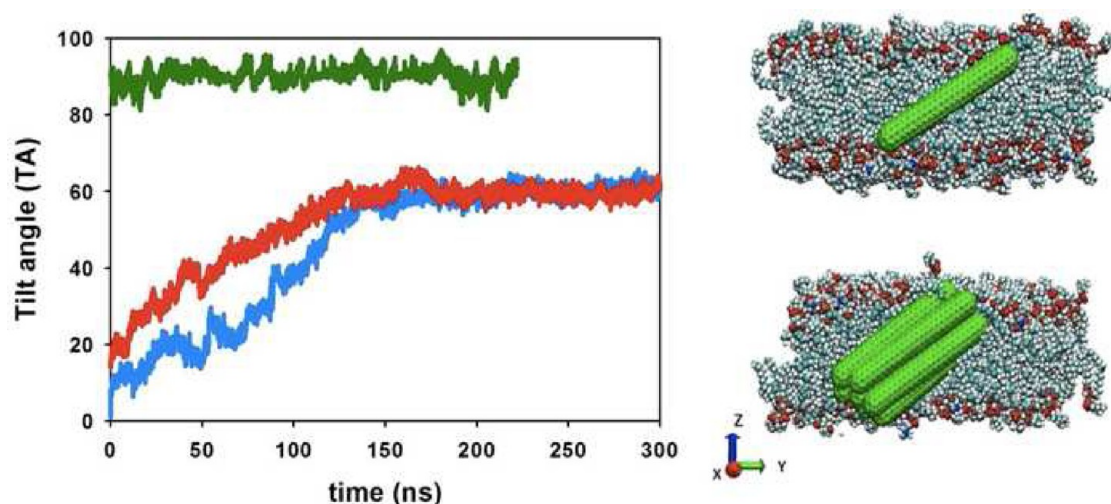


**Figure 4.** Tilt angle (TA) formed between the CNTs embedded in the phospholipid bilayer and the vector normal to the bilayer as a function of simulation time. The three curves are for results obtained for systems B (green), C (blue), and D (red) (see Figure 2 for the respective initial configurations). The two snapshots on the right illustrate the final configurations obtained for systems C and D.

the vector normal to the lipid bilayer ( $Z$  axis). Tilt angles of  $0^\circ$  and  $90^\circ$  indicate that the CNT is perpendicular or parallel to the membrane, respectively. The results in Figure 4 confirm, in part, our expectations. The CNT considered in system B (green line) remains parallel to the bilayer, while both the single CNTs in system C (blue) and the bundle of CNTs in system D (red) change their orientation as the simulation progresses (the tilt angle increases from  $0^\circ$  to  $\sim 60^\circ$ ). Although it is possible that the final configurations shown in Figure 4 correspond to local minima in the free energy landscape, we use them below to quantify how CNTs embedded on a membrane perturb the lipid molecules. This analysis was performed considering the last 20 ns of each simulation, during which the orientation of the embedded CNTs does not change, according to our results. The results in Figure 4 show that the tilt angle at the end of our simulations for system D is equal to that obtained for system C, even though the simulation snapshots suggest that the CNTs are more buried inside the phospholipid bilayer when a bundle is present than when the single CNT is considered. This occurs because the lipid bilayer swells slightly when the bundle is considered, as discussed below. It should also be pointed out that the CNT bundle is slightly distorted compared to the bundle in its initial configuration. Specifically, the individual CNTs within the bundle slide slightly along the bundle axis, apparently in an attempt to maintain the CNT ends near the headgroups of the lipid molecules. It would appear that, although the nanotube ends are repelled by water because of hydrophobic effects, an effective attraction exists between the layer formed by the lipid headgroups within the phospholipid bilayer and the ends of the CNTs. This attraction, which probably is due to steric effects, seems to block the CNTs in the configurations shown in Figure 4.

**Membrane Thickness.** As mentioned above, the presence of the CNTs can, in some cases, swell the lipid bilayers. The membrane thickness is estimated by plotting the density of the choline headgroups of the lipid molecules in the direction perpendicular to the membrane. Two peaks are obtained, representative of the two leaflets of the membrane. The distance between the two peaks is used here to estimate the bilayer thickness. The thickness of the phospholipid bilayer without CNTs (system A) is  $\sim 3.64$  nm. The CNTs are found

to swell the membranes. In Figure 5, we report representative results obtained for system D. The average thickness of the

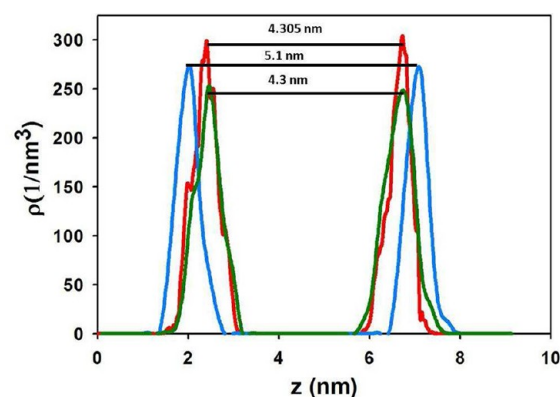


**Figure 5.** Density profiles for the choline group of the lipid molecules in the  $z$  direction perpendicular to the phospholipid bilayer. Results are shown for system D. Red, blue, and green lines represent data obtained averaging all lipid molecules, those lipid molecules found within 0.6 nm from the carbon atoms of the CNTs, and those lipid molecules found farther than 0.6 nm from the CNTs.

bilayer (red line) is  $\sim 4.305$  nm, the thickness of the bilayer obtained considering only the lipid molecules found within 0.6 nm from the carbon atoms of the CNTs increases to 5.1 nm (blue line), and the thickness of the membrane obtained considering only the lipid molecules far from the CNTs is  $\sim 4.3$  nm.

Analogously (results not shown for brevity), the average thickness of the membrane in system C is  $\sim 3.90$  nm ( $\sim 0.26$  nm thicker than the pristine membrane). When only those lipid molecules found within 0.6 nm from the center of the carbon atoms of the CNT are considered, the thickness of the bilayer is  $\sim 4.15$  nm. The average membrane thickness for system B is 4.08 and 4.00 nm near and far from the carbon nanotube, respectively.

**Lipid Molecule Structure within the Phospholipid Bilayers.** The results above show that the CNTs swell the phospholipid membranes. It is expected, as a consequence of

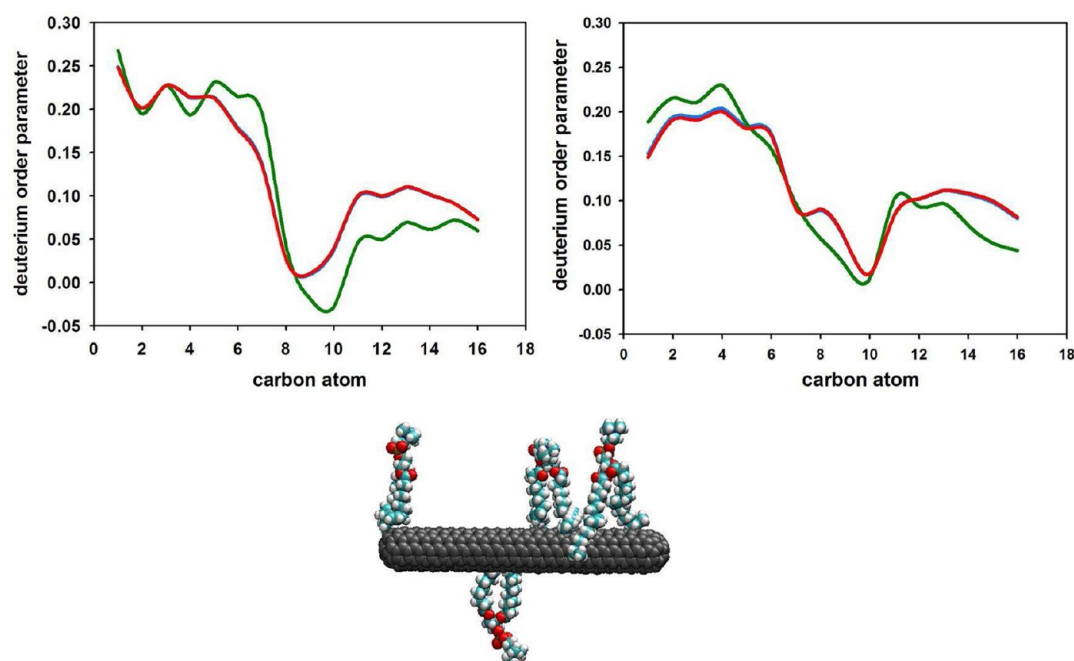


**Figure 6.** Deuterium order parameter for  $sn_1$  and  $sn_2$  DOPC tails (left and right panels, respectively) obtained for system B. Green and red lines are for lipid molecules near and far from the CNT, respectively. Results obtained for lipid molecules in system A (pristine membrane) are shown in blue, but are not visible because they are indistinguishable from the red line. The bottom panel is one snapshot highlighting a few lipid molecules near the CNT.

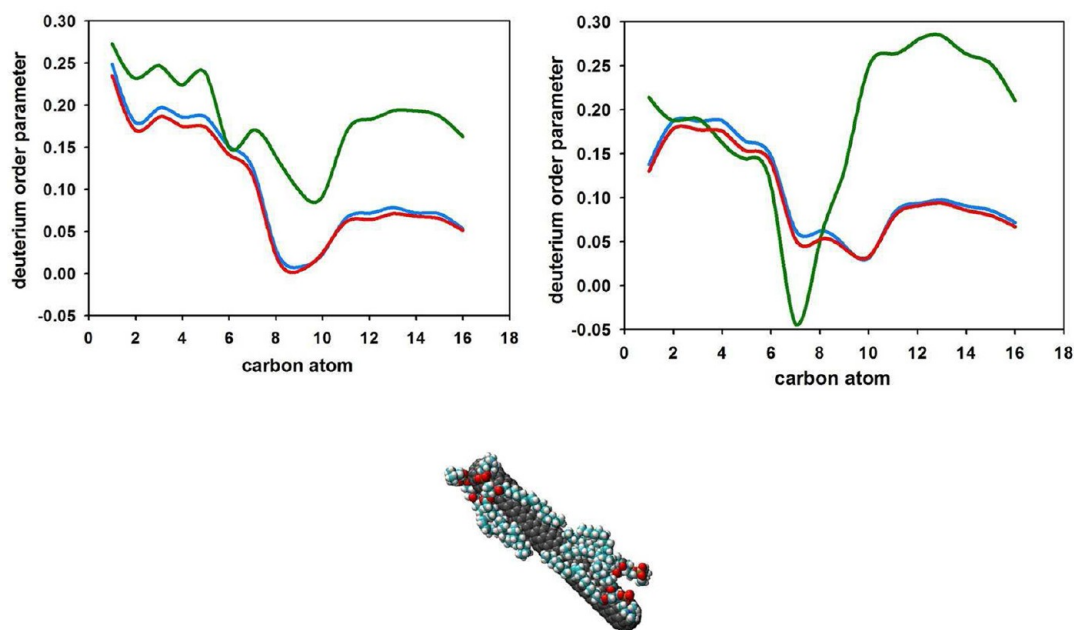


**Figure 7.** Same as Figure 6, but for system C.

both the swelling and the direct interactions between CNTs and the lipid molecules, that local changes in the lipid structure should be pronounced, especially when compared to the lipid structure in the pristine membrane. The local ordering of the lipid molecule is captured by the deuterium order parameter. When the deuterium order parameter is averaged over all lipid molecules within a membrane, the CNTs are not found to have significant effects on the lipid molecule structure. To highlight CNT effects, in the analysis below, we differentiate between lipid molecules that are near, and those that are far from the embedded CNTs. Lipid molecules are considered near the

CNTs when they are found at distances shorter than 0.6 nm from the centers of the carbon atoms of the CNTs.

**System B.** In Figure 6, we compare the deuterium order parameter for the  $sn_1$  and  $sn_2$  tails of the lipid molecules (left and right panels, respectively) far and near the CNT in system B to the results obtained for lipids in the pristine bilayer. To visualize the differences, we report in the bottom panel one simulation snapshot for a few lipids near the CNT. The results show that the lipids far from the CNT do not show a different structure compared to the lipid molecules in the pristine layer (blue and red line are essentially indistinguishable). When the

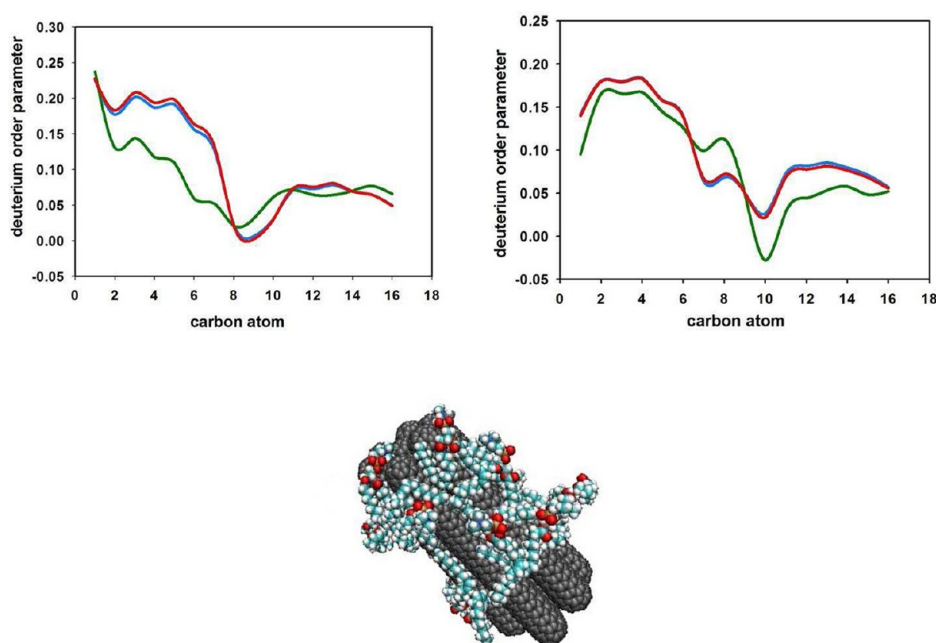


Figure 8. Same as Figure 6, but for system D.

lipid molecules near the CNT are considered (green line), small changes are observed for the deuterium order parameter of both  $sn_1$  and  $sn_2$  tails. The changes are minimal because, in system B, only the end of the DOPC tails is in contact with the CNT.

**System C.** Analogous to results obtained for system B, in Figure 7, we report deuterium order parameter results obtained for system C. The snapshot, provided in the bottom panel, provides evidence according to which the lipid molecules near the CNT are found to adsorb on the CNT surface with their tail groups straightened by the CNT. As a result, the deuterium order parameter increases significantly for the tail groups of the lipid molecules near the CNT (green lines in the top panels). Comparing results for  $sn_1$  and  $sn_2$ , we observe that the order parameter for the latter actually decreases in the presence of the nanotube for carbon atoms C1–C7. This is a consequence of a change in the orientation of the lipid molecules; as they adsorb onto the CNT mostly via the  $sn_1$  tail, they have to induce some disorder in the  $sn_2$  tail, at least in the portion of the tail near the glycerol group. Ordering of  $sn_2$  becomes very pronounced in carbon atoms C8–C16, due to adsorption onto the CNT. Because the CNT considered is rather small, not many lipid molecules are affected by its presence. As in the case of system B, the lipid molecules far from the CNT do not show significant changes in deuterium order parameter compared to those molecules in the pristine phospholipid bilayer.

**System D.** In Figure 8, we report results obtained for lipid molecules in system D. The snapshot illustrates how the lipid molecules adsorb and pack around the bundle of CNTs. The effect is a somewhat less-ordered structure for the lipid molecules near the CNTs. This effect is quantified by the deuterium order parameter results (top panels), which show a decrease in order for the lipid molecules found near the CNTs. It would appear that the CNT bundle disrupts, to some extent, the structure typically observed for lipid molecules in DOPC phospholipid bilayers. As opposed to the results discussed for system C, because the CNT bundle has a significant size, the bundle affects a rather large number of lipid molecules. As in all

other cases considered, the lipid molecules far from the CNT bundle show little, if any, change in structure compared to results obtained for the pristine bilayer.

**End-to-End Distance in DOPC Molecules.** To allow both the changes in membrane thickness and the changes in lipid molecule order, it is necessary that the end-to-end distance within each lipid tail changes in the presence of the CNTs. The end-to-end distance for the chains is calculated here as the distance between the first carbon atom and the last carbon atom (C1–C18) of both the  $sn_1$  and the  $sn_2$  tails of the lipid molecule. The results for the end-to-end distance of the lipid molecule tails for all the systems considered are shown in Table 2, where we distinguish between lipid molecule tails near and

Table 2. End-to-End Distance of the Lipid Molecules

system	DOPC near CNT (nm)	DOPC far from CNT (nm)
B $sn_1$	$1.52 \pm 0.01$	$1.64 \pm 0.02$
B $sn_2$	$1.48 \pm 0.06$	$1.63 \pm 0.03$
C $sn_1$	$1.80 \pm 0.13$	$1.63 \pm 0.04$
C $sn_2$	$1.78 \pm 0.02$	$1.64 \pm 0.02$
D $sn_1$	$1.81 \pm 0.14$	$1.59 \pm 0.03$
D $sn_2$	$1.77 \pm 0.15$	$1.60 \pm 0.02$

far from the CNTs. For comparison, the end-to-end distances for  $sn_1$  and  $sn_2$  tails obtained for the lipid molecules in the pristine DOPC membrane are  $\sim 1.63 \pm 0.04$  and  $1.60 \pm 0.02$  nm, respectively.

For system B, the lipids near the CNT appear to be compressed compared with those lipids far from the CNT. Simulation snapshots suggest that the tails of the lipid molecules bend to accommodate the CNT. In systems C and D, our results show that the lipid molecules near the CNTs are more extended by  $\sim 0.15$ – $0.20$  nm compared with the lipid molecules far from the CNTs. These results are due to the interaction between the CNT surfaces and the lipid molecules that adsorb onto them, in some cases, leading to straightened chains (see, for example, Figure 7). The end-to-end distances



for the lipid molecules far from the CNTs in both systems C and D do not differ significantly compared to results obtained in pristine DOPC bilayers.

**Lipid Packing Structure Within the Bilayers.** In Figure 9, we plot the two-dimensional radial distribution function

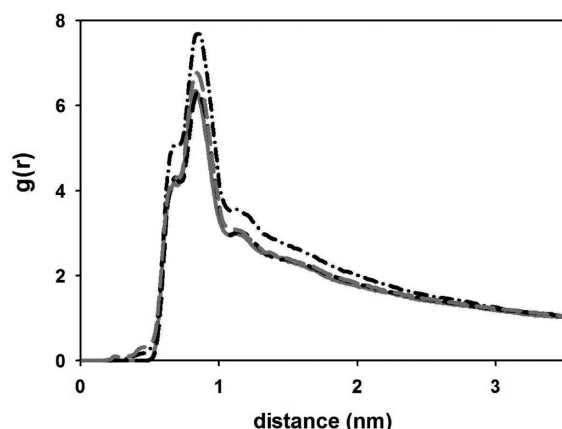


**Figure 9.** Two-dimensional radial distribution function calculated among the lipid headgroups for systems A (gray continuous), B (black dashed), C (gray dashed), and D (black dashed-dotted).

calculated among the nitrogen atoms of the choline headgroups. The results are shown for systems A (gray continuous line), B (black dashed), C (gray dashed), and D (black dashed-dotted line). The results for systems A and B do not differ from each other, suggesting that one CNT embedded parallel to the phospholipid membrane does not affect the lateral packing of the lipids. The results for systems C and D are also very similar to those obtained for the pristine membrane, although the intensity of the first peak in the radial distribution function is larger compared with the one observed for systems A and B. This qualitative observation suggests a slightly more pronounced packing of the lipid molecules when the CNTs are tilted with respect to the membrane vertical. As discussed later, this is probably due to the adsorption of the lipid molecules near the CNTs.

The radial distribution functions show limited differences among the four systems considered. Analyzing Voronoi tessellation diagrams,<sup>90</sup> we can attain additional insights.

We obtain Voronoi tessellation plots by analyzing the position of the centers of mass of the lipid headgroups within the four membranes considered, and by comparing the results to the position of the CNTs. In Figure 10, we show the results obtained for the pristine membrane (system A). The lipid molecules are uniformly distributed within the membrane, in qualitative agreement with data reported by Qiao et al.<sup>58</sup>

One representative Voronoi tessellation diagram and one simulation snapshot obtained for system B are shown in Figure 11. For clarity, the simulation box is replicated twice along both directions. The position of the CNT is highlighted by the blue rectangle. The distribution of the lipid headgroups within the membrane does not seem to differ substantially compared to results obtained for the pristine membrane. Similar observations can be repeated for system C (Figure 12), with the only difference being that the lipid headgroups are farther from each other where the CNT pierces the membrane (red circle). It would also appear that the lipid molecules in the second shell near the CNT pack closely to the lipid molecules adsorbed onto the CNT. This is possible because, as shown from the thickness of the lipid bilayer, some of the adsorbed lipids are stretched into the aqueous solution. The results obtained for system D (Figure 13) show a more pronounced effect of the CNTs onto the structure of the lipid molecules. Because the CNT bundle is relatively large in size when compared to a single CNT, the region depleted of lipid molecules corresponding to where the bundle pierces the phospholipid membrane becomes very evident in the Voronoi tessellation plot. It also appears that the lipid molecules are farther from each other within the entire surface above the CNT bundle, which is due to steric effects evidenced in Figure 8, above. All observations from Voronoi tessellation analysis suggest that the two-dimensional packing of the DOPC molecules within the membrane is perturbed by the tilted CNTs, but only near the tubes. The effects are more pronounced for the CNT bundle, as expected.

**Surface Area per Lipid Molecule.** The results for the radial distribution function do not show significant changes in

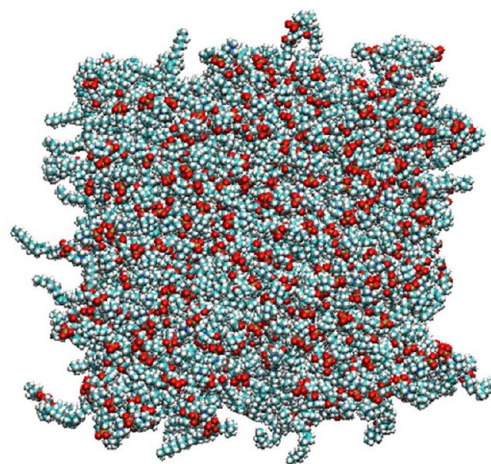
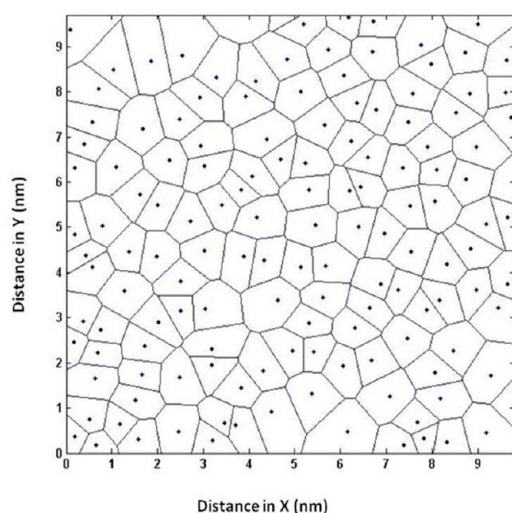


**Figure 10.** Representative Voronoi tessellation for system A (left), and top view of a simulation snapshot for the same system (right).



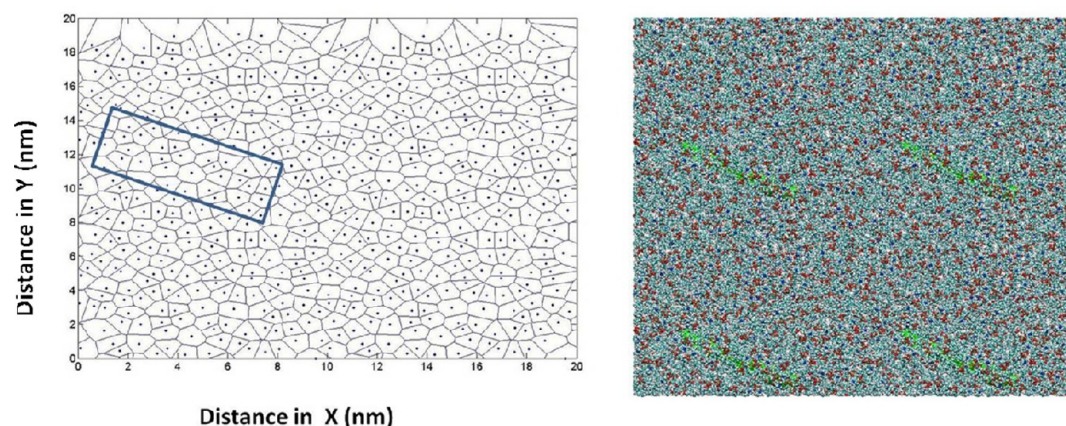


**Figure 11.** Same as Figure 10, but for system B. The blue rectangle on the left panel indicates the position of the CNT embedded within the phospholipid membrane. The CNT is shown as green in the simulation snapshot. The simulation box is replicated twice in the X and twice in the Y direction for clarity.

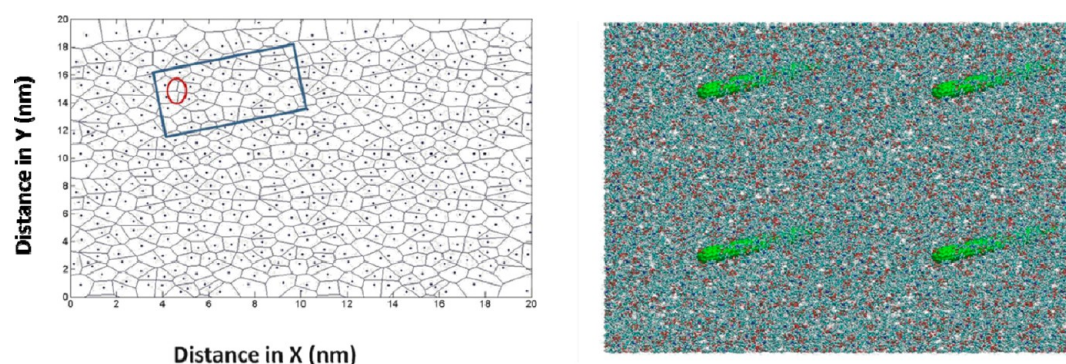


**Figure 12.** Same as Figure 11, but for system C. The red circle on the left panel indicates the region where the CNT pierces the phospholipid membrane.

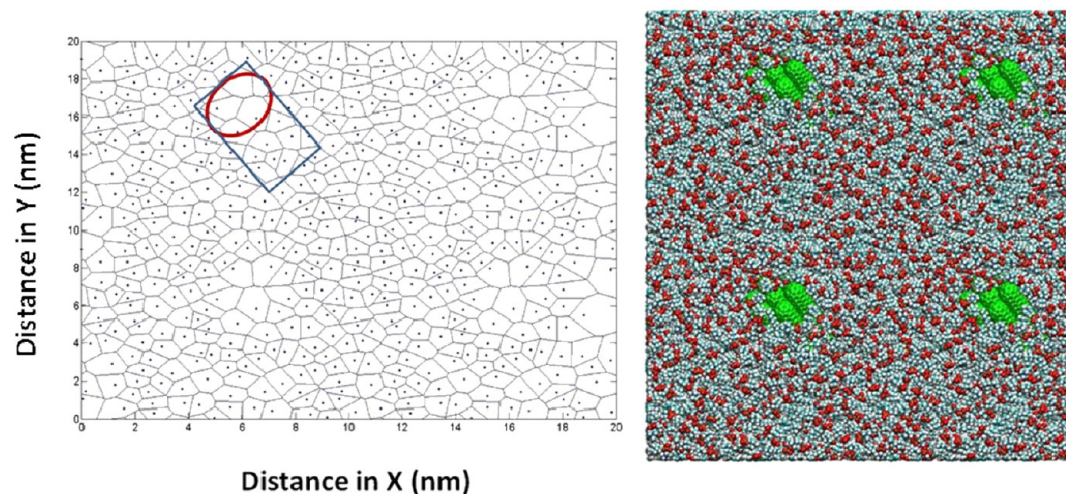


**Figure 13.** Same as Figure 12, but for system D.

the packing of lipid molecules. However, the Voronoi tessellation results suggest changes in lipid packing, especially near the CNTs. To quantify eventual changes, we compare the surface area per lipid molecule. The results are  $70.0 \pm 0.2 \text{ \AA}^2$  in system A (as mentioned above),  $68.71 \pm 0.06 \text{ \AA}^2$  in system B,  $71.02 \pm 0.12 \text{ \AA}^2$  in system C, and  $74.20 \pm 0.07 \text{ \AA}^2$  in system D. It would appear that the area per lipid molecule increases noticeably compared with that of the pristine membrane only

for system D, in which case, a bundle of seven CNTs is embedded in the membrane. This could be important for drug-delivery applications. Although both membrane thickness and surface area per headgroup have been found to be related to water permeability across a phospholipid membrane, Mathai et al.<sup>91</sup> suggested that the area per headgroup is the most important parameter (the larger the area per headgroup, the higher water permeability). Although our results show that the

perturbation on the lipid bilayer structure due to the presence of CNTs embedded within the phospholipid bilayer is not uniform, the fact that the area per lipid molecule changes suggests that the permeability of the phospholipid membranes could be affected by the presence of carbon nanotubes.

**Mobility of the DOPC Molecules.** To address the mechanical response of the membrane to the presence of the embedded CNTs in Figure 14, we report results for the two-

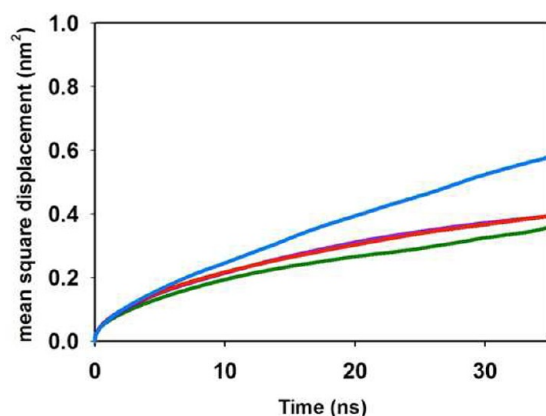


**Figure 14.** Two-dimensional mean-square displacement for lipid molecules in systems A (blue), B (green), C (purple), and D (red) as a function of simulation time.

dimensional mean-square displacement of the lipids in the four systems considered as a function of time. From the slope of the mean-square displacement at long observation times, the self-diffusion coefficient can be estimated. The results below have been estimated by considering the mean-square displacement obtained from 20 to 35 ns of observation time. For the pristine membrane, we estimate the self-diffusion coefficient to be  $\sim 3.15 \pm 0.3 \times 10^{-8} \text{ cm}^2/\text{s}$ , which is in reasonable agreement with the literature value of  $3.13 \times 10^{-8} \text{ cm}^2/\text{s}$ .<sup>82</sup> In general, the presence of the embedded CNTs is found to slow down the mobility of the lipid molecules. Structural data have suggested that system B does not differ substantially compared to the pristine DOPC membrane. On the contrary, diffusion data suggest that the larger the number of lipid molecules that are in contact with the CNTs, the more pronounced the effect is on the lateral self-diffusion coefficient. The estimated lateral self-diffusion coefficients for lipid molecules in systems B, C, and D are  $1.53 \pm 0.1 \times 10^{-8}$ ,  $1.35 \pm 0.1 \times 10^{-8}$ , and  $1.48 \pm 0.1 \times 10^{-8} \text{ cm}^2/\text{s}$ , respectively. These data suggest that the embedded CNTs could significantly affect the membrane mechanical properties.

**Structure of Interfacial Water.** The results above, in particular, the distribution of lipids within the membrane revealed by the Voronoi tessellation diagrams, suggest the possibility that the embedded CNTs might affect the structure of interfacial water. As the most pronounced differences are expected for system D (a bundle of CNTs embedded in the membrane), we study in detail the structure of interfacial water on that system and we compare it to the one observed near the pristine phospholipid bilayer (system A).

To calculate the density of oxygen atoms of water in the direction perpendicular to the membrane, we implement the algorithm proposed by Bhide and Berkowitz.<sup>92</sup> In short, for each water molecule, the algorithm searches for the nearest lipid molecule. The vertical distance between the water

molecule and the phosphorus atom of the lipid headgroup is used as the vertical position of the water molecule. The results in Figure 15 are obtained for interfacial water in systems A and

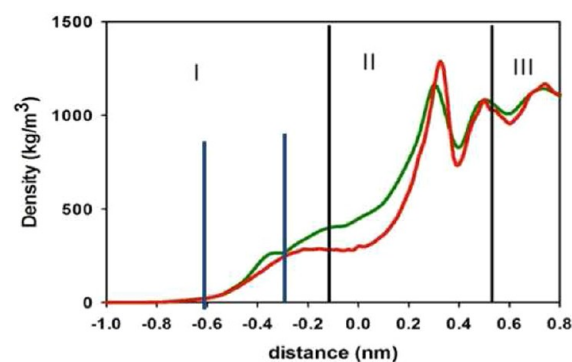


**Figure 15.** Density of oxygen atoms of water molecules in the direction perpendicular to the phospholipid bilayer. Results are shown for water in systems A and D (red and green lines, respectively). See text for distinction between regions I, II, and III. The vertical lines in region I highlight the position of the water molecules analyzed in Figures 16 and 17.

D (red and green lines, respectively). In system D, we only consider those water molecules near the CNTs. The density profiles are divided into regions I, II, and III. Water in region I is found in the vicinity of the carbonyl groups of the lipid headgroups. Water in region II is found near the phosphocholine groups. Most of the interfacial water is found in region III, which corresponds to the second hydration shell near a headgroup. The results for system A are consistent with those reported in the literature.<sup>92</sup> Compared to results on the pristine membrane, the presence of the CNT bundle yields an increase in the water density within region II. This increase in water density is related to the increase of the area per lipid molecule observed in system D compared to the pristine membrane, as discussed above and shown in Figure 13.

To complement the analysis of interfacial water, in Figure 16, we report the planar density distribution of water molecules within a layer with a thickness of 0.3 nm above the lipid tail groups. The position of this layer is identified in Figure 15. The results are shown only for system D. The large area near the center of the figure depleted of water molecules is where the CNT bundle pierces the phospholipid membrane. In this region, not only the CNTs push away water molecules because of steric effects but also the lipid molecules adsorbed onto the CNT bundle are elevated with respect to the surrounding lipids (the thickness of the membrane is larger near the CNTs than far from them), leading to a further decrease in the water density. A pictorial visualization of these effects is provided in Figure 17, where we show representative simulation snapshots for the water molecules near the CNT bundle used to obtain the density profile of Figure 16, viewed from above the membrane (left) and from the side (center). We also show the lipid molecules that, adsorbed onto the CNTs, push away interfacial water molecules (right). We conclude that the embedded CNT bundle affects the interfacial water associated with the headgroups of the lipid molecules, possibly affecting the membrane permeability to small-molecular-weight compounds.



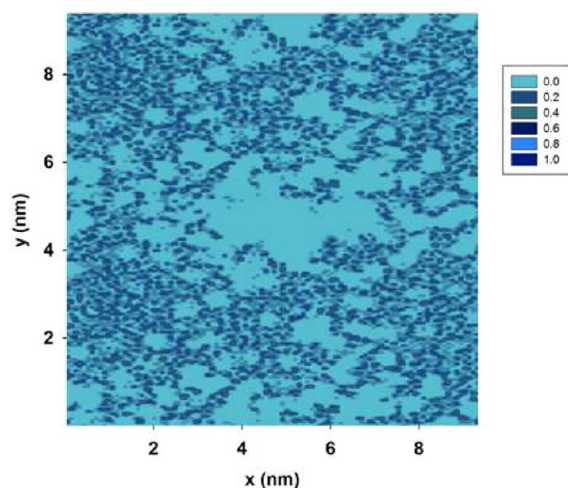


**Figure 16.** Planar density distribution of water molecules found within a layer of thickness 0.3 nm above the lipid tail groups. Only oxygen atoms of water molecules are considered for these calculations. Results are shown only for system D. Densities are expressed in number of molecules per nm<sup>3</sup>.

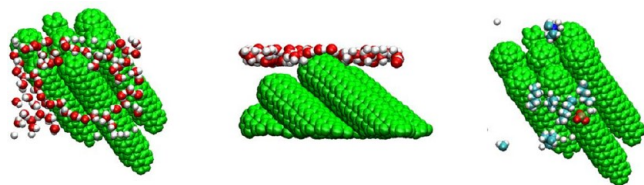


**Figure 17.** Representative simulation snapshots for interfacial water molecules used to obtain the density profile of Figure 16. We provide a top (left) and a side view (middle) of such water molecules. In the right panel, we show the lipid molecules that, adsorbed onto the CNT bundle, contribute to remove water molecules from the interfacial region.

#### 4. CONCLUSIONS

In summary, using classical atomistic molecular dynamics simulations, we studied how (5,5) carbon nanotubes with a length of 6 nm embedded in a DOPC phospholipid membrane affect the structure, packing, and dynamics of the lipid molecules. In all cases considered, the membrane swells due to the presence of the nanotubes, in particular, when a bundle of seven nanotubes is found within the membrane. When one nanotube is parallel to the membrane and located at its center, only small structural differences are observed compared to the pristine membrane. Significant changes in the structure of individual lipid molecules as well as in their two-dimensional packing are observed when either one isolated nanotube or a bundle of seven nanotubes is tilted and embedded within the membrane. These results are due to the adsorption of lipid molecules on the hydrophobic surfaces of the nanotubes. In all cases, however, the effects are very short-ranged and become almost negligible at distances larger than  $\sim 1$  nm from the nanotube. It was found that the effects on the self-diffusion coefficient of the lipid molecules due to the embedded carbon nanotubes are very pronounced and lead to a decreased mobility of the lipid molecules due to preferential interactions with the carbon nanotubes. The perturbation on the structure of the lipid molecules near the nanotubes also leads to perturbation in the structure of interfacial water molecules,

suggesting that the presence of carbon nanotubes tilted within the phospholipid membrane might affect the permeation of various molecular compounds across the membrane.

#### AUTHOR INFORMATION

##### Corresponding Author

\*E-mail: [astriolo@ou.edu](mailto:astriolo@ou.edu).

##### Notes

The authors declare no competing financial interest.

#### ACKNOWLEDGMENTS

This work was supported, in part, by the U.S. National Science Foundation, under Award Number CBET-0853759. Generous allocations of computing time were provided by the Oklahoma Supercomputer Center for Education and Research (OSCCER) and by the National Energy Research Scientific Computing Center (NERSC). NERSC is supported by the Office of Science of the U.S. Department of Energy under Contract No. DE-AC02-05CH11231.

#### REFERENCES

- (1) Bianco, A. Carbon nanotubes for the delivery of therapeutic molecules. *Expert Opin. Drug Delivery* **2004**, *1*, 57–65.
- (2) Kostarelos, K.; Bianco, A.; Prato, M. Promises, facts and challenges for carbon nanotubes in imaging and therapeutics. *Nat. Nanotechnol.* **2009**, *4*, 627–633.
- (3) Chen, X.; Kis, A.; Zettl, A.; Bertozzi, C. R. A cell nanoinjector based on carbon nanotubes. *Proc. Natl. Acad. Sci. U.S.A.* **2007**, *104*, 8218–8222.
- (4) Moyon, C. M.; Kostarelos, K.; Prato, M.; Bianco, A. Functionalized carbon nanotubes for probing and modulating molecular functions. *Chem. Biol.* **2010**, *17*, 107–115.
- (5) Haddon, R. C. Carbon nanotubes. *Acc. Chem. Res.* **2002**, *35*, 997.
- (6) Wu, W.; Wieckowski, S.; Pastorin, G.; Benincasa, M.; Klumpp, C.; Briand, J. P.; Gennaro, R.; Prato, M.; Bianco, A. Targeted delivery of amphotericin B to cells by using functionalized carbon nanotubes. *Angew. Chem., Int. Ed.* **2005**, *44*, 6358–6362.
- (7) Samori, C.; Boucetta, H. A.; Sainz, R.; Guo, C.; Toma, F.; Fabbro, C.; da Ros, T.; Prato, M.; Kostarelos, K.; Bianco, A. Enhanced anticancer activity of multi-walled carbon nanotube-methotrexate conjugates using cleavable linkers. *Chem. Commun.* **2010**, *46*, 1494–1496.
- (8) Kam, N. W. S.; Liu, Z.; Dai, H. Carbon nanotubes as intracellular transporters for proteins and DNA: An investigation of the uptake mechanism and pathway. *Angew. Chem., Int. Ed.* **2006**, *45*, 577–581.
- (9) Herrero, M. A.; Toma, F. M.; Jamal, K. T. A.; Kostarelos, K.; Bianco, A.; Ros, T. D.; Bano, F.; Casalis, L.; Scoles, G.; Prato, M. Synthesis and characterization of a carbon nanotube–dendron series for efficient siRNA delivery. *J. Am. Chem. Soc.* **2009**, *131*, 9843–9848.
- (10) Podesta, J. E.; Jamal, K. T. A.; Herrero, M. A.; Tian, B.; Ali, H. B.; Hegde, V.; Bianco, A.; Prato, M.; Kostarelos, K. Antitumor activity and prolonged survival by carbon-nanotube-mediated therapeutic siRNA silencing in a human lung xenograft model. *Small* **2009**, *5*, 1176–1185.
- (11) Singh, R.; Pantarotto, D.; McCarthy, D.; Chaloin, O.; Hoebeke, J.; Partidos, C. D.; Charalambos, D.; Briand, J. P.; Prato, M.; Bianco, A.; et al. Binding and condensation of plasmid DNA onto functionalized carbon nanotubes: Toward the construction of nanotube-based gene delivery vectors. *J. Am. Chem. Soc.* **2005**, *127*, 4388–4396.
- (12) Kostarelos, K.; Lacerda, L.; Pastorin, G.; Wu, W.; Wieckowski, S.; Luangsivilay, J.; Godefroy, S.; Pantarotto, D.; Briand, J. P.; Muller, S.; et al. Cellular uptake of functionalized carbon nanotubes is independent of functional group and cell type. *Nat. Nanotechnol.* **2007**, *2*, 108–113.

- (13) Jamal, K. T. A.; Nerl, H.; Muller, K. H.; Boucetta, H. A.; Li, S.; Shouping, H.; Peter, D.; Jinschek, D. J. R.; Prato, M.; Bianco, A.; et al. Cellular uptake mechanisms of functionalised multi-walled carbon nanotubes by 3D electron tomography imaging. *Nanoscale* **2011**, *3*, 2627–2635.
- (14) Porter, A. E.; Gass, M.; Muller, K.; Skepper, J. N.; Midgley, P. A.; Welland, M. Direct imaging of single-walled carbon nanotubes in cells. *Nat. Nanotechnol.* **2007**, *2*, 713–717.
- (15) Cheng, J.; Fernando, K. A. S.; Veca, L. M.; Sun, Y. P.; Lamond, A. I.; Lam, Y. W.; Cheng, S. H. Reversible accumulation of PEGylated single-walled carbon nanotubes in the mammalian nucleus. *ACS Nano* **2008**, *2*, 2085–2094.
- (16) Allen, B. L.; Kichambare, P. D.; Gou, P.; Vlasova, I. I.; Kapralov, A. A.; Konduru, N.; Kagan, V. E.; Star, A. Biodegradation of single-walled carbon nanotubes through enzymatic catalysis. *Nano Lett.* **2008**, *8*, 3899–3903.
- (17) Allen, B. L.; Kotchey, G. P.; Chen, Y.; Yanamala, N. V. K.; Seetharaman, J. K.; Kagan, V. E.; Star, A. Mechanistic investigations of horseradish peroxidase-catalyzed degradation of single-walled carbon nanotubes. *J. Am. Chem. Soc.* **2009**, *131*, 17194–17205.
- (18) Liu, X.; Hurt, R. H.; Kane, A. B. Biodurability of single-walled carbon nanotubes depends on surface functionalization. *Carbon* **2010**, *48*, 1961–1969.
- (19) Russier, J.; Moyon, C. M.; Venturelli, E.; Gravel, E.; Marcolongo, G.; Meneghetti, M.; Doris, E.; Bianco, A. Oxidative biodegradation of single- and multi-walled carbon nanotubes. *Nanoscale* **2011**, *3*, 893–896.
- (20) Zhao, Y.; Allen, B. L.; Star, A. Enzymatic degradation of multiwalled carbon nanotubes. *J. Phys. Chem. A* **2011**, *115*, 9536–9544.
- (21) Kagan, V. E.; Konduru, N. V.; Feng, W.; Allen, B. L.; Conroy, J.; Volkov, Y.; Vlasova, I. I.; Belikova, N. A.; Yanamala, N.; Kapralov, A.; et al. Carbon nanotubes degraded by neutrophil myeloperoxidase induce less pulmonary inflammation. *Nat. Nanotechnol.* **2010**, *5*, 354–359.
- (22) Bianco, A.; Kostarelos, K.; Prato, M. Making carbon nanotubes biocompatible and biodegradable. *Chem. Commun.* **2011**, *47*, 10182–10188.
- (23) Shvedova, A. A.; Castranova, V.; Kisin, E. R.; Schwegler-Berry, D.; Murray, A. R.; Gandelsman, V. Z.; Maynard, A.; Baron, P. Exposure to carbon nanotube material: Assessment of nanotube cytotoxicity using human keratinocyte cells. *J. Toxicol. Environ. Health, Part A* **2003**, *66*, 1909–1926.
- (24) Manna, S. K.; Sarkar, S.; Barr, J.; Wise, K.; Barrera, E. V.; Jejelowo, O.; Ficht, A. C. R.; Ramesh, G. T. Single-walled carbon nanotube induces oxidative stress and activates nuclear transcription factor- $\kappa$ B in human keratinocytes. *Nano Lett.* **2005**, *5*, 1676–1684.
- (25) Lam, C. W.; James, J. T.; McCluskey, R.; Hunter, R. L. Pulmonary toxicity of single-wall carbon nanotubes in mice 7 and 90 days after intratracheal instillation. *Toxicol. Sci.* **2004**, *77*, 126–134.
- (26) Chen, X.; Tam, U. C.; Czapinski, J. L.; Lee, G. S.; Rabuka, D.; Zettl, A.; Bertozzi, C. R. Interfacing carbon nanotubes with living cells. *J. Am. Chem. Soc.* **2006**, *128*, 6292–6293.
- (27) Jia, G.; Wang, H.; Yan, L.; Wang, X.; Pei, R.; Yan, T.; Zhao, Y.; Guo, X. Cytotoxicity of carbon nanomaterials: Single-wall nanotube, multi-wall nanotube, and fullerene. *Environ. Sci. Technol.* **2005**, *39*, 1378–1383.
- (28) Dumortier, H.; Lacotte, S.; Pastorin, G.; Marega, R.; Wu, W.; Bonifazi, D.; Briand, J. P.; Prato, M.; Muller, S.; Bianco, A. Functionalized carbon nanotubes are non-cytotoxic and preserve the functionality of primary immune cells. *Nano Lett.* **2006**, *6*, 1522–1528.
- (29) Wick, P.; Manser, P.; Limbach, L. K.; Weglikowska, U. D.; Krumeich, F.; Roth, S.; Stark, W. J.; Bruinink, A. The degree and kind of agglomeration affect carbon nanotube cytotoxicity. *Toxicol. Lett.* **2007**, *168*, 121–131.
- (30) Zhu, Y.; Ran, T.; Li, Y.; Guo, J.; Li, W. Dependence of the cytotoxicity of multi-walled carbon nanotubes on the culture medium. *Nanotechnology* **2006**, *17*, 4668–4674.
- (31) Crouzier, T.; Nimmagadda, A.; Nollert, M. U.; McFetridge, P. S. Modification of single walled carbon nanotube surface chemistry to improve aqueous solubility and enhance cellular interactions. *Langmuir* **2008**, *24*, 13173–13181.
- (32) Mutlu, G. M.; Budinger, G. R. S.; Green, A. A.; Urich, D.; Soberanes, S.; Chiarella, S. E.; Alheid, G. F.; McCrimmon, D. R.; Szleifer, I.; Hersam, M. C. Biocompatible nanoscale dispersion of single-walled carbon nanotubes minimizes in vivo pulmonary toxicity. *Nano Lett.* **2010**, *10*, 1664–1670.
- (33) Kang, S.; Mauter, M. S.; Elimelech, M. Microbial cytotoxicity of carbon-based nanomaterials: Implications for river water and wastewater effluent. *Environ. Sci. Technol.* **2009**, *43*, 2648–2653.
- (34) Kang, S.; Herzberg, M.; Rodrigues, D. F. Antibacterial effects of carbon nanotubes: Size does matter! *Langmuir* **2008**, *24*, 6409–6413.
- (35) Vecitis, C. D.; Zodrow, K. R.; Kang, S.; Elimelech, M. Electronic-structure-dependent bacterial cytotoxicity of single-walled carbon nanotubes. *ACS Nano* **2010**, *4*, 5471–5479.
- (36) Liu, S.; Wei, L.; Hao, L.; Fang, N.; Chang, M. W.; Xu, R.; Yang, Y.; Chen, Y. Sharper and faster “nano darts” kill more bacteria: A study of antibacterial activity of individually dispersed pristine single-walled carbon nanotubes. *ACS Nano* **2009**, *3*, 3891–3902.
- (37) Porter, A. E.; Gass, M.; Bendall, J. S.; Muller, K.; Goode, A.; Skepper, J. N.; Midgley, P. A.; Welland, M. Uptake of noncytotoxic acid-treated single-walled carbon nanotubes into the cytoplasm of human macrophage cells. *ACS Nano* **2009**, *3*, 1485–1492.
- (38) Singh, P.; Samori, C.; Toma, F. M.; Bussy, C.; Nunes, A.; Jamal, K. T. A.; Moyon, C. M.; Prato, M.; Kostarelos, K.; Bianco, A. Polyamine functionalized carbon nanotubes: Synthesis, characterization, cytotoxicity and siRNA binding. *J. Mater. Chem.* **2011**, *21*, 4850–4860.
- (39) Yeagle, P. L. *The Structure of Biological Membranes*, 2nd ed.; CRC Press: Boca Raton, FL, 2005.
- (40) Pack, D. W.; Hoffman, A. S.; Pun, S.; Stayton, P. S. Design and development of polymers for gene delivery. *Nature* **2005**, *4*, 581–593.
- (41) Jenssen, H.; Hamill, P.; Hancock, R. E. W. Peptide antimicrobial agents. *Clin. Microbiol. Rev.* **2006**, *19*, 491–511.
- (42) Brogden, K. A. Antimicrobial peptides: Pore formers or metabolic inhibitors in bacteria? *Nature* **2005**, *3*, 238–250.
- (43) Plank, C.; Zauner, W.; Wagner, E. Application of membrane-active peptides for drug and gene delivery across cellular membranes. *Adv. Drug Delivery Rev.* **1998**, *34*, 21–35.
- (44) Lasic, D. D.; Papahadjopoulos, D. *Medical Applications of Liposomes*; Elsevier Science: Amsterdam, 1998.
- (45) Hou, W.-C.; Moghadam, B. Y.; Westerhoff, P.; Posner, J. D. Distribution of fullerenes nanomaterials between water and model biological membranes. *Langmuir* **2011**, *27*, 11899–11905.
- (46) Jamal, W. T. A.; Kostarelos, K. Liposomes: From a clinically established drug delivery system to a nanoparticle platform for theranostic nanomedicine. *Acc. Chem. Res.* **2011**, *44*, 1094–1104.
- (47) Rasch, M. R.; Rossinyol, E.; Hueso, J. L.; Goodfellow, B. W.; Arbiol, J.; Korgel, B. A. Hydrophobic gold nanoparticle self-assembly with phosphatidylcholine lipid: Membrane-loaded and Janus vesicles. *Nano Lett.* **2010**, *10*, 3733–3739.
- (48) Lopez, C. F.; Nielsen, S. O.; Moore, P. B.; Klein, M. L. Understanding nature’s design for a nanosyringe. *Proc. Natl. Acad. Sci. U.S.A.* **2004**, *101*, 4431–4434.
- (49) Yang, K.; Ma, Y. Q. Computer simulation of the translocation of nanoparticles with different shapes across a lipid bilayer. *Nat. Nanotechnol.* **2010**, *5*, 579–583.
- (50) Vácha, R.; Veracoechea, F. J. M.; Frenkel, D. Receptor-mediated endocytosis of nanoparticles of various shapes. *Nano Lett.* **2011**, *11*, 5391–5395.
- (51) Redmill, P. S.; McCabe, C. Molecular dynamics study of the behavior of selected nanoscale building blocks in a gel-phase lipid bilayer. *J. Phys. Chem. B* **2010**, *114*, 9165–9172.
- (52) Ionescu, T. C.; Qi, F.; McCabe, C.; Striolo, A.; Kieffer, J.; Cummings, P. T. Evaluation of force fields for molecular simulation of polyhedral oligomeric silsesquioxanes. *J. Phys. Chem. B* **2006**, *110*, 2502–2510.



- (53) Song, B.; Yuan, H.; Jameson, C. J.; Murad, S. Permeation of nanocrystals across lipid membranes. *Mol. Phys.* **2011**, *109*, 1511–1526.
- (54) Wallace, E. J.; Sansom, M. S. P. Blocking of carbon nanotube based nanoinjectors by lipids: A simulation study. *Nano Lett.* **2008**, *8*, 2571–2756.
- (55) D’Rozario, R. S. G.; Wee, C. L.; Wallace, E. J.; Sansom, M. S. P. The interaction of C<sub>60</sub> and its derivatives with a lipid bilayer via molecular dynamics simulations. *Nanotechnology* **2009**, *20*, 115102.
- (56) Jusufi, A.; DeVane, R. H.; Shinoda, W.; Klein, M. L. Nanoscale carbon particles and the stability of lipid bilayers. *Soft Matter* **2011**, *7*, 1139.
- (57) Bedrov, D.; Smith, G. D.; Davande, H.; Li, L. Passive transport of C<sub>60</sub> fullerenes through a lipid membrane: A molecular dynamics simulation study. *J. Phys. Chem. B* **2008**, *112*, 2078–2084.
- (58) Qiao, R.; Roberts, A. P.; Mount, A. S.; Klaine, S. J.; Stephen, J.; Ke, P. C. Translocation of C<sub>60</sub> and its derivatives across a lipid bilayer. *Nano Lett.* **2007**, *7*, 614–619.
- (59) Ekkabut, J. W.; Baoukina, S.; Triampo, W.; Tang, I. M.; Tieleman, D. P.; Monticelli, L. Computer simulation study of fullerene translocation through lipid membranes. *Nat. Nanotechnol.* **2008**, *3*, 363–368.
- (60) Pogodin, S.; Baulin, V. A. Can a nanotube pierce through a phospholipid bilayer? *ACS Nano* **2010**, *4*, 5293–5300.
- (61) Shaul, A. B.; Szleifer, I.; Gelbart, W. M. Chain organization and thermodynamics in micelles and bilayers. I. Theory. *J. Chem. Phys.* **1985**, *83*, 3597–3611.
- (62) Pogodin, S.; Slater, N. K. H.; Baulin, V. A. Surface patterning of carbon nanotubes can enhance their penetration through a phospholipid bilayer. *ACS Nano* **2011**, *5*, 1141–1146.
- (63) Hoefinger, S.; Franco, M. M.; Gallo, T.; Cantelli, A.; Calvaresi, M.; Gomes, J. A. N. F.; Zerbetto, F. A computational analysis of the insertion of carbon nanotubes into cellular membranes. *Biomaterials* **2011**, *32*, 7079–7085.
- (64) Kar, P.; Seel, M.; Weidemann, T.; Hoefinger, S. Theoretical mimicry of biomembranes. *FEBS Lett.* **2009**, *583*, 1909–1915.
- (65) Groot, R. D.; Warren, P. B. Dissipative particle dynamics: Bridging the gap between atomistic and mesoscopic simulation. *J. Chem. Phys.* **1997**, *107*, 4423–4435.
- (66) Wang, H.; Michelssens, S.; Moors, S. L. C.; Ceulemans, A. Molecular dynamics study of dipalmitoylphosphatidylcholine lipid layer self-assembly onto a single-walled carbon nanotube. *Nano Res.* **2009**, *2*, 945–954.
- (67) Lin, S.; Blankschtein, D. Role of the bile salt surfactant sodium cholate in enhancing the aqueous dispersion stability of single-walled carbon nanotubes: A molecular dynamics simulation study. *J. Phys. Chem. B* **2010**, *114*, 15616–15625.
- (68) Wallace, E. J.; Sansom, M. S. P. Carbon nanotube self-assembly with lipids and detergent: A molecular dynamics study. *Nanotechnology* **2009**, *20*, 045101.
- (69) Tummala, N. R.; Striolo, A. SDS Surfactants on carbon nanotubes: Aggregate morphology. *ACS Nano* **2009**, *3*, 595–602.
- (70) Suttipong, M.; Tummala, N. R.; Kitiyanan, B.; Striolo, A. Role of surfactant molecular structure on self-assembly: Aqueous SDBS on carbon nanotubes. *J. Phys. Chem. C* **2011**, *115*, 17286–17296.
- (71) Richard, C.; Balavoine, F.; Schultz, P.; Ebbesen, T. W.; Mioskowski, C. Supramolecular self-assembly of lipid derivatives on carbon nanotubes. *Science* **2003**, *300*, 775–778.
- (72) Warschawski, D. E.; Devaux, P. F. Order parameters of unsaturated phospholipids in membranes and the effect of cholesterol: A <sup>1</sup>H–<sup>13</sup>C solid-state NMR study at natural abundance. *Eur. Biophys. J.* **2005**, *34*, 987–996.
- (73) Liu, Y.; Nagle, J. F. Diffuse scattering provides material parameters and electron density profiles of biomembranes. *Phys. Rev. E: Stat., Nonlinear, Soft Matter Phys.* **2004**, *69*, 040901.
- (74) Goetz, R.; Lipowsky, R. Computer simulations of bilayer membranes: Self-assembly and interfacial tension. *J. Chem. Phys.* **1998**, *108*, 7397–7409.
- (75) Thakkar, F. M.; Ayappa, K. G. Melting and mechanical properties of polymer grafted lipid bilayer membranes. *J. Chem. Phys.* **2011**, *135*, 104901.
- (76) Damodaran, K. V.; Merz, K. M., Jr. A comparison of DMPC- and DLPE-based lipid bilayers. *Biophys. J.* **1994**, *66*, 1076–1087.
- (77) Risselada, H. J.; Marrink, S. J. Curvature effects on lipid packing and dynamics in liposomes revealed by coarse grained molecular dynamics simulations. *Phys. Chem. Chem. Phys.* **2009**, *11*, 2056–2067.
- (78) Song, K. C.; Livanec, P. W.; Klauda, J. B.; Kuczera, K.; Dunn, R. C.; Im, W. Orientation of fluorescent lipid analogue BODIPY-PC to probe lipid membrane properties: Insights from molecular dynamics simulations. *J. Phys. Chem. B* **2011**, *115*, 6157–6165.
- (79) Lim, J. B.; Klauda, J. B. Lipid chain branching at the iso- and anteiso-positions in complex chlamydia membranes: A molecular dynamics study. *Biochim. Biophys. Acta, Biomembr.* **2011**, *1808*, 323–331.
- (80) Vanegas, J. M.; Longo, M. L.; Faller, R. C. Ordered and disordered lipid membranes: Convergence of stress profiles due to ergosterol. *J. Am. Chem. Soc.* **2011**, *133*, 3720–3723.
- (81) Skaug, M. J.; Longo, M. L.; Faller, R. The impact of Texas red on lipid bilayer properties. *J. Phys. Chem. B* **2011**, *115*, 8500–8505.
- (82) Siu, S. W. I.; Vacha, R.; Jungwirth, P.; Boeckmann, R. A. Biomolecular simulations of membranes: Physical properties from different force fields. *J. Chem. Phys.* **2008**, *128*, 125103.
- (83) Nagle, S. T.; Petrache, H. I.; Nagle, J. F. Structure and interactions of fully hydrated dioleoylphosphatidylcholine bilayers. *Biophys. J.* **1998**, *75*, 917–925.
- (84) Berendsen, H. J. C.; Grigerat, J. R.; Straatsma, T. P. The missing term in effective pair potentials. *J. Phys. Chem.* **1987**, *91*, 6269–6271.
- (85) Walther, J. H.; Jaffe, R. L.; Kotsalis, E. M.; Werder, T.; Halicioglu, T.; Koumoutsakos, P. Hydrophobic hydration of C<sub>60</sub> and carbon nanotubes in water. *Carbon* **2004**, *42*, 1185–1194.
- (86) Steele, W. A.; Cheng, A. Computer simulation of ammonia on graphite. II. Monolayer melting. *J. Chem. Phys.* **1990**, *92*, 3867–3873.
- (87) Darden, T.; York, D.; Pedersen, L. Particle mesh Ewald: An N<sub>log</sub>(N) method for Ewald sums in large systems. *J. Chem. Phys.* **1993**, *98*, 10089–10092.
- (88) Tieleman, D. P.; Marrink, S. J.; Berendsen, H. J. C. A computer perspective of membranes: Molecular dynamics studies of lipid bilayer systems. *Biochim. Biophys. Acta* **1997**, *1331*, 235–270.
- (89) Vermeer, L. S.; de Groot, B. L.; Reat, V.; Milton, A.; Cazplicki, J. Acyl chain order parameter profiles in phospholipid bilayers: Computation from molecular dynamics simulations and comparison with <sup>2</sup>H NMR experiments. *Eur. Biophys. J.* **2007**, *36*, 919–931.
- (90) Aurenhammer, F. Voronoi diagrams – A survey of a fundamental geometric data structure. *Comput. Surv.* **1991**, *23*, 345–405.
- (91) Mathai, J. C.; Nagle, S. T.; Nagle, J. F.; Zeidel, M. L. Structural determinants of water permeability through the lipid membrane. *J. Gen. Physiol.* **2008**, *131*, 69–76.
- (92) Bhidé, S. Y.; Berkowitz, M. L. Structure and dynamics of water at the interface with phospholipid bilayers. *J. Chem. Phys.* **2005**, *123*, 224702.